

# RFormer: Transformer-based Generative Adversarial Network for Real Fundus Image Restoration on A New Clinical Benchmark

Zhuo Deng<sup>1,\*</sup>, Yuanhao Cai<sup>1,\*</sup>, Lu Chen<sup>2</sup>, Zheng Gong<sup>1</sup>,  
Qiqi Bao<sup>1</sup>, Xue Yao<sup>2</sup>, Dong Fang<sup>2</sup>, Shaochong Zhang<sup>2,†</sup>, Lan Ma<sup>1,†</sup>

<sup>1</sup> Shenzhen International Graduate School, Tsinghua University, <sup>2</sup> Shenzhen Eye Hospital

## Abstract

Ophthalmologists have used fundus images to screen and diagnose eye diseases. However, different equipments and ophthalmologists pose large variations to the quality of fundus images. Low-quality (LQ) degraded fundus images easily lead to uncertainty in clinical screening and generally increase the risk of misdiagnosis. Thus, real fundus image restoration is worth studying. Unfortunately, real clinical benchmark has not been explored for this task so far. In this paper, we investigate the real clinical fundus image restoration problem. Firstly, We establish a clinical dataset, Real Fundus (RF), including 120 low- and high-quality (HQ) image pairs. Then we propose a novel Transformer-based Generative Adversarial Network (RFormer) to restore the real degradation of clinical fundus images. The key component in our network is the Window-based Self-Attention Block (WSAB) which captures non-local self-similarity and long-range dependencies. To produce more visually pleasant results, a Transformer-based discriminator is introduced. Extensive experiments on our clinical benchmark show that the proposed RFormer significantly outperforms the state-of-the-art (SOTA) methods. In addition, experiments of downstream tasks such as vessel segmentation and optic disc/cup detection demonstrate that our proposed RFormer benefits clinical fundus image analysis and applications. The dataset, code, and models will be released.

## 1. introduction

Due to the safety and cost-effectiveness in acquiring, fundus images are widely used by ophthalmologists for early eye disease detection and diagnosis, including glaucoma [11, 43, 49, 54], diabetic retinopathy [24, 29, 48], cataract [15, 76], and age-related macular degeneration [2, 51]. However, different equipments and ophthalmologists pose large variations to the quality of fundus images. A screening study of 5,575 patients found that about 12% of

\* = equal contribution, † = corresponding author

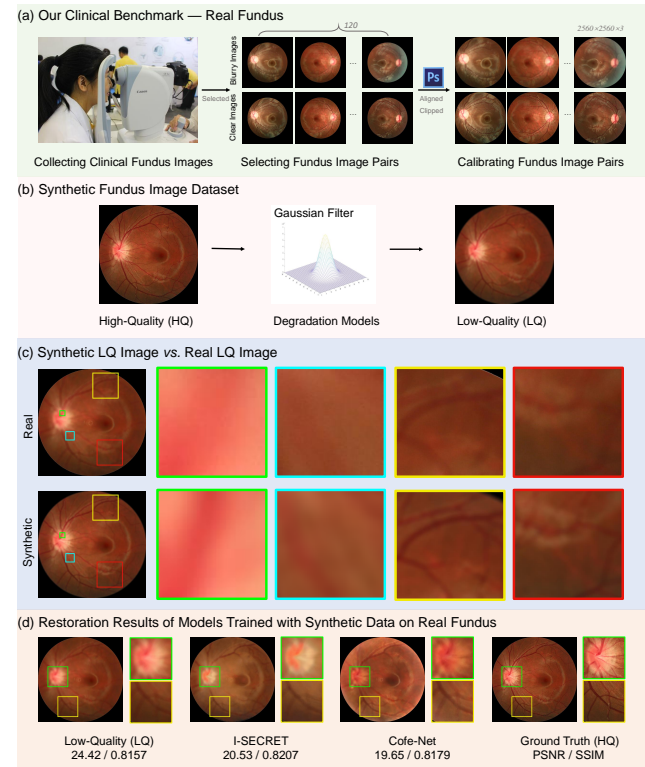


Figure 1. **Our Real Fundus vs. Synthetic Dataset.** (a) The pipeline of establishing our clinical fundus image benchmark, Real Fundus (RF). (b) Artificial degradation models are used to synthesize low-quality (LQ) fundus images from their high-quality (HQ) counterparts. (c) Comparisons of the synthetic LQ fundus image and our real clinical LQ image. (d) Restoration results of models trained with synthetic data on RF. The two CNN-based methods, I-SECRET [13] and Cofe-Net [58], fail to recover the LQ images.

fundus images are of inadequate quality to be readable by ophthalmologists [52]. We analyze the factors causing the degradation in real fundus image capturing. **Firstly**, patients, especially infant patients, do not cooperate with the capturing process of fundus images. Specifically, most patients are reluctant to undergo pupil dilation, which causes

poorly lit and blurred fundus images. Besides, infant patients usually can not resist the eye-closing reflex caused by a bright light during flash photography. **Secondly**, in practice, spatial pixel misalignment, color, and brightness mismatch are inevitable due to the changes in light conditions and misoperations of inexperienced Ophthalmologists. **Thirdly**, high-quality (HQ) fundus images can be collected in hospitals of developed areas using high-precision fundus cameras. However, these equipments are expensive and unaffordable for hospitals in some remote areas of under-developed or developing countries. As a result, low-precision and portable fundus cameras are used to capture low-quality (LQ) fundus images. These LQ fundus images easily mislead the clinical diagnosis and lead to unsatisfactory results of downstream tasks like blood vessels segmentation. Various markers and biomarkers of the retina (*e.g.*, hemorrhage, microaneurysm, exudate, optic nerve and cup) are essential in different diseases. Hence, it is necessary to ensure the prominence and visibility of each marker for precise clinical diagnosis. Thus, when LQ fundus images are captured, ophthalmologists often repeat dozens of shots until HQ fundus images are obtained. Nonetheless, this repeated capturing process harms patients, degrades hospital efficiency, prevents reliable diagnosis of ophthalmologists, and impacts automated image analysis systems.

We observe the clinical fundus images and find that the main degradation types of LQ images include out-of-focus blur, motion blur, artifact, over-exposure, and over-darkness. Compared with other types of degradation, blur, especially out-of-focus blur, poses the most severe threat to image analysis and clinical diagnosis. An example is shown in Fig. 2, where the uneven illumination, haze, and out-of-focus blur are presented in (a), (b), and (c). It can be observed that the performance of blood vessel segmentation only collapses on out-of-focus blurred fundus images.

Traditional fundus image restoration methods [18, 31] are mainly based on hand-crafted priors. These model-based methods achieve unsatisfactory performance and generality due to the poor representing capacity. Recently, deep Convolutional Neural Networks (CNNs) have been applied to learn the end-to-end mapping function of fundus image restoration. Although impressive results have been achieved, the CNN-based methods [13, 45, 47, 56, 58, 68, 78] show limitations in capturing long-range dependencies. In recent years, the natural language processing (NLP) model, Transformer [63] has been introduced into computer vision and outperformed CNN methods in many tasks. The Multi-head Self-Attention (MSA) module in Transformer excels at modeling non-local similarity and long-range dependencies. This advantage of Transformer may provide a possibility to address the limitations of CNN-based methods.

Existing deep learning methods rely on a large amount of LQ and HQ fundus image pairs. Unfortunately, real clinical

benchmark has not been explored for fundus image reconstruction. There remains a data-hungry problem. As shown in Fig. 1 (b), to get more image pairs, artificial degradation models such as Gaussian filter are used to synthesize LQ fundus images from their HQ counterparts. However, as depicted in Fig. 1 (c), artificial degradation is fundamentally different from clinical degradation. As shown in Fig. 1 (d), the two CNN-based methods [13, 58] trained with synthesized data fail in real fundus image restoration.

In this paper, we investigate the real fundus image restoration problem, which has not been studied in the literature. Our work is the first attempt. To begin with, we establish a clinical benchmark, Real Fundus (RF), including 120 LQ and HQ real clinical fundus image pairs to alleviate the data-hungry issue. Based on this dataset, we propose a novel method, namely Transformer-based Generative Adversarial Network (RFormer), for real fundus image restoration. Specifically, the generator and discriminator are built up by the basic unit, Window-based Self-Attention Blocks (WSABs). The self-attention mechanism equipped with each basic block excels at capturing the non-local self-similarity and long-range dependencies, which are the main limitations of existing CNN-based methods. In particular, the generator adopts a U-shape structure to aggregate multi-resolution contextual information. Unlike previous CNN-based Generative Adversarial Networks (GANs), we adopt a Transformer-based discriminator to extract non-local image prior information and thus improve the ability of discriminator to distinguish restored fundus images from the ground-truth HQ fundus images. Our Transformer-based adversarial training scheme encourages the generator to create more plausible-looking natural and visually-pleasant images with more detailed contents and structural textures.

Our contributions can be summarized as follows:

- We establish a new clinical benchmark, RF, to evaluate fundus image restoration algorithms in real clinical scenes. To the best of our knowledge, this is the first real fundus image dataset in the literature.
- We propose a novel Transformer-based method, RFormer, for real fundus image restoration. To the best of our knowledge, it is the first attempt to explore the potential of Transformer for this task in the literature.
- Comprehensive experiments demonstrate that our RFormer significantly outperforms SOTA algorithms. Extensive experiments of downstream tasks further validate the effectiveness of our method.

## 2. related work

### 2.1. Fundus Image Restoration

Traditional fundus image restoration and enhancement methods [18, 31] are mainly based on hand-crafted priors.

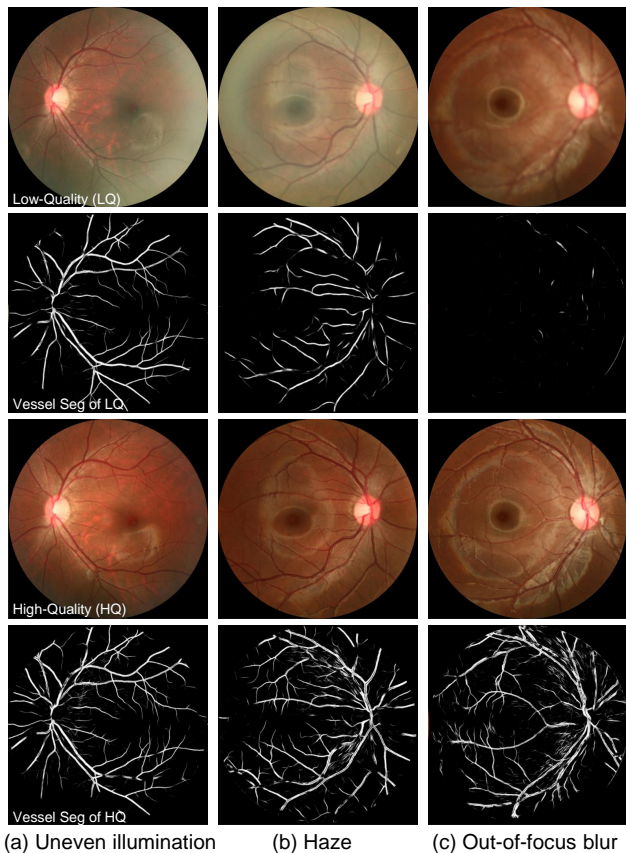


Figure 2. **Fundus images of different degeneration types and their blood vessel segmentation results.** (a) Uneven illumination. (b) Haze. (c) Out-of-focus blur. From top to bottom are the low-quality (LQ) fundus images, blood vessel segmentation of the LQ fundus images, the ground-truth high-quality (HQ) fundus images, and blood vessel segmentation of the HQ fundus images.

For example, Setiawan *et al.* [57] apply contrast limited adaptive histogram equalization (CLAHE) to fundus image enhancement. Some methods [21, 50, 64] decompose the reflection and illumination, achieving image enhancement and correction by estimating the solution in an alternate minimization scheme. However, these model-based methods achieve unsatisfactory performance and generality due to the poor representing capacity. With the development of deep learning, fundus image restoration has witnessed a significant progress. CNNs [13, 45, 47, 56, 58, 68, 78] apply a powerful learning model to restore LQ fundus images. For instance, Zhao *et al.* [78] propose an end-to-end deep CNN to remove the lesions on the fundus images of cataract patients. However, the cataract lesions are not caused by clinical fundus imaging. Sourya *et al.* [56] and Shen *et al.* [58] customize different synthetic degradation models to better simulate the degradation types in actual clinical practice. However, real fundus image degradation

is more sophisticated than synthesized degradation. It is hard to simulate real degradation by artificial degradation models completely. Thus, models trained on synthesized data easily fail in real fundus image restoration. In addition, the CNN-based methods show limitations in capturing non-local self-similarity and long-rang dependencies, which are critical for fundus image reconstruction.

## 2.2. Generative Adversarial Network

Generative Adversarial Network (GAN) is firstly introduced in [23] and has been proven successful in image synthesis [22, 32, 81], and translation [32, 81]. Subsequently, GAN is applied to image restoration and enhancement, *e.g.*, super resolution [3, 26, 28, 37, 56, 65, 78], deraining [53], enlighten [35, 73], dehazing [25, 27, 40], image inpainting [74, 79], style transfer [38, 81], image editing [71, 72], and mobile photo enhancement [12, 75]. Although GAN is widely applied in low-level vision, few works are dedicated to improving the underlying framework of GAN, such as replacing the traditional CNN framework with Transformer. Jiang *et al.* [34] propose the first Transformer-based GAN, TransGAN, for image generation. Nonetheless, to the best of our knowledge, the Transformer-based GAN has not been involved in fundus image restoration.

## 2.3. Vision Transformer

Transformer is firstly proposed by [63] for machine translation. Recently, Transformer has achieved great success in high-level vision, such as image classification [1, 16, 17, 44, 69], semantic segmentation [7, 44, 69, 80], human pose estimation [5, 6, 39, 41, 46, 70], object detection [9, 14, 30, 44, 82], *etc.* Due to the advantage of capturing long-range dependencies and excellent performance in many high-level vision tasks, Transformer has also been introduced into low-level vision [8, 10, 42, 67]. SwinIR [42] uses Swin Transformer [44] blocks to build up a residual network and achieve SOTA results in natural image restoration. Chen *et al.* [10] propose a large model IPT pre-trained on large-scale datasets with a multitask learning scheme. MST [4] presents a spectral-wise Transformer for hyper-spectral image reconstruction. Although Transformer has achieved impressive results in many tasks, its potential in fundus image restoration remains under-explored.

## 3. Methodology

### 3.1. RFormer Architecture

The architecture of RFormer is shown in Fig. 3, where (a) and (b) depict the generator and discriminator. Fig. 3 (c) shows the proposed Window-based Self-Attention Blocks (WSABs), which consists of a Feed-Forward Network (FFN) (detailed in Fig. 3 (d)), a Window-based Multi-head Self-Attention (W-MSA), and two layer normalization.

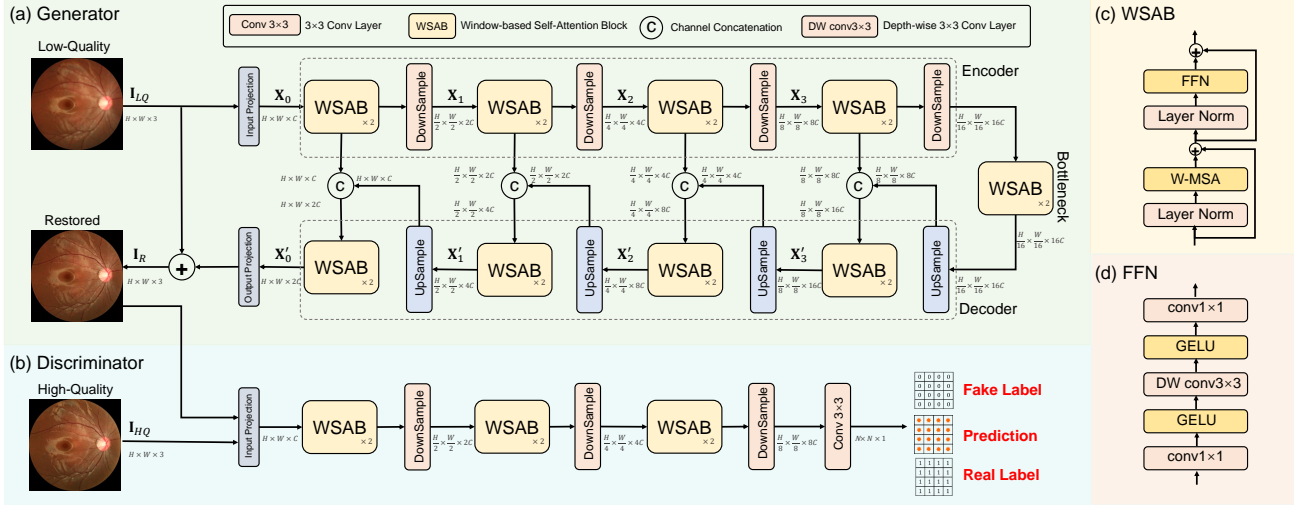


Figure 3. **Architecture of our RFormer.** (a) The generator adopts a U-shaped structure, including an encoder, a bottleneck, and a decoder. (b) Different from CNN-based GANs, our discriminator is Transformer-based. (c) The basic unit of our RFormer is Window-based Multi-head Self-Attention Block (WSAB). (d) FFN consists of two  $1 \times 1$  *conv* layers, two GLEU activations, and a depth-wise  $3 \times 3$  *conv* layer.

The generator adopts a U-shaped [55] architecture including an encoder, a bottleneck, and a decoder. The input LQ image is denoted as  $\mathbf{I}_{LQ} \in \mathbb{R}^{H \times W \times 3}$ . **Firstly**, the generator exploits a projection layer consisting of a  $3 \times 3$  convolution (*conv*) and LeakyReLU to extract shallow feature  $\mathbf{I}_0 \in \mathbb{R}^{H \times W \times C}$ . **Secondly**, 4 encoder stages are used for deep feature extraction on  $\mathbf{I}_0$ . Each stage is composed of two consecutive WSABs and one downsampling layer. We adopt a  $4 \times 4$  *conv* with stride 2 as the downsampling layer to downscale the spatial size of feature maps and double the channel dimension. Thus, the feature of the  $i$ -th stage in the encoder is denoted as  $\mathbf{X}_i \in \mathbb{R}^{\frac{H}{2^i} \times \frac{W}{2^i} \times 2^i C}$ . Here,  $i = 0, 1, 2, 3$  indicates the four stages. **Thirdly**,  $\mathbf{X}_3$  undergoes the bottleneck that consists of two WSABs. **Subsequently**, following the spirits of U-Net, we customize a symmetrical decoder, which also contains 4 stages. Each stage of the decoder is also composed of two WSABs and one upsampling layer. Similarly, the feature maps of the  $i$ -th stage in the decoder is denoted as  $\mathbf{X}'_i \in \mathbb{R}^{\frac{H}{2^i} \times \frac{W}{2^i} \times 2^{i+1} C}$ . The upsampling layer is a bilinear interpolation followed by a  $3 \times 3$  *conv* layer. To alleviate the information loss caused by downsampling in the encoder, skip connections are used for feature fusion between the encoder and decoder. **Finally**, after undergoing the decoder, the feature maps pass through a  $3 \times 3$  *conv* layer to generate a residual image  $\mathbf{I}' \in \mathbb{R}^{H \times W \times 3}$ . Subsequently, the restored fundus image can be obtained by  $\mathbf{I}_R = \mathbf{I}_{LQ} + \mathbf{I}'$ .

As shown in Fig. 3 (b), the discriminator aims to distinguish the restored fundus images from ground-truth high-quality fundus images. As analyzed in [32], patch-level GAN is more effective than image-level GAN in capturing high-resolution and fine-grained image information,

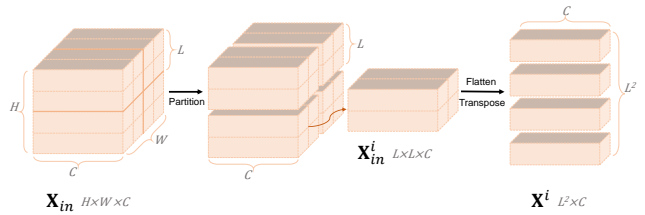


Figure 4. **Illustration of the feature map partition.** The feature maps are partitioned into non-overlapping windows, where the window-based multi-head self-attention (W-MSA) is conducted.

which is critical for restoring clinical fundus image restoration. Hence, we follow the adversarial training scheme based on image patches as PatchGAN and further propose a Transformer-based discriminator. More specifically, the discriminator employs the same architecture as the encoder in the generator followed by a  $3 \times 3$  *conv* layer. The restored fundus image  $\mathbf{I}_R \in \mathbb{R}^{H \times W \times 3}$  concatenated with the ground-truth HQ fundus image  $\mathbf{I}_{HQ} \in \mathbb{R}^{H \times W \times 3}$  undergoes our proposed Transformer-based discriminator to generate the predicted map  $\mathbf{F} \in \mathbb{R}^{N \times N \times 1}$ .

### 3.2. Window-based Self-Attention Block

The emergence of Transformer provides an alternative to address the limitations of CNN-based methods in modeling non-local self-similarity and long-range dependencies. However, as analyzed in Swin Transformer [44], the computational cost of the standard global Transformer is quadratic to the spatial size of the input feature ( $HW$ ). This burden is nontrivial and sometimes unaffordable. To tackle this problem, we adopt the Window-based Multi-

head Self-Attention (W-MSA) [44] as the self-attention mechanism and integrate it with the basic Transformer unit. The computational complexity of W-MSA is linear to the spatial size, which is much cheaper than that of standard global MSA. The components of our proposed Window-based Multi-head Self-Attention Block (WSAB) are shown in Fig. 3 (c). WSAB consists of a W-MSA, an FFN, and two layer normalization. The details of FFN are shown in Fig. 3 (d). Then WSAB can be formulated as

$$\begin{aligned}\mathbf{F}' &= \text{W-MSA}(\text{LN}(\mathbf{F}_{in})) + \mathbf{F}_{in}, \\ \mathbf{F}_{out} &= \text{FFN}(\text{LN}(\mathbf{F}')) + \mathbf{F}',\end{aligned}\quad (1)$$

where  $\mathbf{F}_{in}$  represents the input feature maps of a WSAB.  $\text{LN}(\cdot)$  represents the layer normalization.  $\mathbf{F}'$  and  $\mathbf{F}_{out}$  denote the output feature of W-MSA and FFN respectively.

### 3.2.1 Window-based Multi-head Self-Attention

Instead of using global correspondence, we partition the feature map into non-overlapping windows. Subsequently, the token interactions are calculated inside each window. As shown in Fig. 4, given the input feature map  $\mathbf{X}_{in} \in \mathbb{R}^{H \times W \times C}$  with  $H$  and  $W$  being the height and the width. We partition  $\mathbf{X}_{in}$  into  $L \times L$  non-overlapping windows. The feature of the  $i$ -th window is denoted as  $\mathbf{X}_{in}^i \in \mathbb{R}^{L \times L \times C}$ , where  $i \in \{1, 2, \dots, N\}$  and  $N = HW/L^2$ .  $\mathbf{X}_{in}^i$  is flattened and transposed into  $\mathbf{X}^i \in \mathbb{R}^{L^2 \times C}$ . We conduct MSA on  $\mathbf{X}^i$ . Firstly,  $\mathbf{X}^i$  is linearly projected into *query*  $\mathbf{Q}^i$ , *key*  $\mathbf{K}^i$ , and *value*  $\mathbf{V}^i \in \mathbb{R}^{L^2 \times C}$ :

$$\mathbf{Q}^i = \mathbf{X}^i \mathbf{W}^Q, \mathbf{K}^i = \mathbf{X}^i \mathbf{W}^K, \mathbf{V}^i = \mathbf{X}^i \mathbf{W}^V, \quad (2)$$

where  $\mathbf{W}^Q, \mathbf{W}^K, \mathbf{W}^V \in \mathbb{R}^{C \times C}$  are learnable parameters, denoting the projection matrices of the *query*, *key* and *value*. We respectively split  $\mathbf{Q}^i$ ,  $\mathbf{K}^i$  and  $\mathbf{V}^i$  into  $k$  heads along the channel dimension:  $\mathbf{Q}^i = [\mathbf{Q}_1^i, \dots, \mathbf{Q}_k^i]$ ,  $\mathbf{K}^i = [\mathbf{K}_1^i, \dots, \mathbf{K}_k^i]$  and  $\mathbf{V}^i = [\mathbf{V}_1^i, \dots, \mathbf{V}_k^i]$ . The dimension of each head is  $d_k = C/k$ . The Self-Attention (SA) for head  $j$  is formulated as

$$\text{SA}(\mathbf{Q}_j^i, \mathbf{K}_j^i, \mathbf{V}_j^i) = \text{softmax}\left(\frac{\mathbf{Q}_j^i \mathbf{K}_j^{iT}}{\sqrt{d_k}}\right) \mathbf{V}_j^i, \quad (3)$$

where  $\mathbf{Q}_j^i$ ,  $\mathbf{K}_j^i$  and  $\mathbf{V}_j^i$  respectively represent the *query*, *key* and *value* of head  $j$  respectively. The output tokens  $\mathbf{X}_o^i \in \mathbb{R}^{L^2 \times C}$  of the  $i$ -th window can be obtained by

$$\mathbf{X}_o^i = \text{Concat}\left(\text{SA}(\mathbf{Q}_j^i, \mathbf{K}_j^i, \mathbf{V}_j^i)\right)_{j=1}^k \mathbf{W}^O + \mathbf{B}, \quad (4)$$

where  $\text{Concat}(\cdot)$  denotes the concatenating operation,  $\mathbf{B} \in \mathbb{R}^{L^2 \times C}$  represents the position embedding, and  $\mathbf{W}^O \in \mathbb{R}^{C \times C}$  are learnable parameters. We reshape  $\mathbf{X}_o^i$  to obtain the output window feature map  $\mathbf{X}_{out}^i \in \mathbb{R}^{L \times L \times C}$ . Finally, we merge all the patch representations  $\{\mathbf{X}_{out}^1, \mathbf{X}_{out}^2, \mathbf{X}_{out}^3, \dots, \mathbf{X}_{out}^N\}$  to obtain the output feature maps  $\mathbf{X}_{out} \in \mathbb{R}^{H \times W \times C}$ .

### 3.2.2 Feed-Forward Network

As illustrated in Fig. 3 (d), the Feed-Forward Network (FFN) is composed of a  $1 \times 1$  *conv* layer with a GELU activation, a depth-wise  $3 \times 3$  *conv* layer with a GELU activation, and another  $1 \times 1$  *conv* layer.

### 3.3. Loss Functions

During the training procedure, we exploit the weighted sum of four loss functions as the overall training objective. They are described and analyzed in the following part.

#### 3.3.1 Charbonnier Loss

The first loss function is the Charbonnier loss between the restored and ground-truth HQ images:

$$\mathcal{L}_1(\mathbf{I}_R, \mathbf{I}_{HQ}) = \sqrt{\|\mathbf{I}_R - \mathbf{I}_{HQ}\|^2 + \varepsilon^2} \quad (5)$$

where  $\mathbf{I}_R$  denotes the restored fundus image,  $\mathbf{I}_{HQ}$  represents the ground-truth HQ fundus image, and  $\varepsilon$  denotes a constant which is empirically set to  $10^{-3}$  in experiments.

#### 3.3.2 Fundus Quality Perception Loss

Unlike natural images, fundus images have specific acquisition process and anatomical structures. This indicates fundus images have highly similar styles. Therefore, we exploit high-level feature constraints to improve the perceptual quality and encourage the network to capture the fundus anatomical structures and styles. To this end, we propose Fundus Quality Perception Loss (FQPLoss). More specifically, we adopt VGG-19 [59] as the perception network and pre-train it on the fundus image quality evaluation dataset, Eye-Q [20] with the fundus image quality classification task. The Eye-Q dataset has 28,792 fundus images with three-level quality grading. The perception network trained on the Eye-Q dataset is capable of extracting the difference of high-level features between different qualities of fundus images. Then our FQPLoss can be formulated as

$$\mathcal{L}_{fqp} = \frac{1}{HW} \sum_{i=1}^H \sum_{j=1}^W (\phi(\mathbf{I}_R)(i, j) - \phi(\mathbf{I}_{HQ})(i, j))^2 \quad (6)$$

where  $H$  and  $W$  denote the height and width of the fundus image.  $\phi(\cdot)$  denotes the feature extraction function of the pre-trained perception network. Our FQPLoss is customized to assess a solution with respect to perceptually relevant characteristics. By minimizing the FQPLoss  $\mathcal{L}_{fqp}$ , the model is encouraged to capture more high-level discriminative features and generate more visually-pleasant results.

#### 3.3.3 Adversarial Loss

Our proposed Transformer-based discriminator aims to distinguish the restored fundus images from ground-truth HQ fundus images. More specifically, the discriminator outputs

a patch score map  $\mathbf{F} \in \mathbb{R}^{N_H \times N_W \times 1}$ , where  $N_H$  and  $N_W$  denote the height and width. The score of each position indicates how realistic the corresponding fundus image patch is. Then the adversarial loss is formulated as

$$\begin{aligned}\mathcal{L}_{adv}^D &= \frac{1}{N_H \times N_W} \sum_{i=1}^{N_H \times N_W} (D(\mathbf{I}_R)[i])^2 + (D(\mathbf{I}_{HQ})[i] - 1)^2, \\ \mathcal{L}_{adv}^G &= \frac{1}{N_H \times N_W} \sum_{i=1}^{N_H \times N_W} (D(\mathbf{I}_R)[i] - 1)^2,\end{aligned}\quad (7)$$

where  $D(\cdot)$  denotes the mapping function of our Transformer-based discriminator.  $\mathcal{L}_{adv}^G$  trains the generator to fool the discriminator by generating more realistic restored images. In contrast,  $\mathcal{L}_{adv}^D$  encourages the discriminator to distinguish the restored images from HQ images.

### 3.3.4 Edge Loss

To enhance the high-frequency edge details, we exploit the edge loss function that focuses on the gradient information of images and enhances edge textures. To be specific, the edge loss function is formulated as

$$\mathcal{L}_{edge}(\mathbf{I}_R, \mathbf{I}_{HQ}) = \sqrt{\|\Delta(\mathbf{I}_R) - \Delta(\mathbf{I}_{HQ})\|^2 + \varepsilon^2}, \quad (8)$$

where  $\Delta(\cdot)$  represents the Laplacian operator.

### 3.3.5 The Overall Loss Function

Finally, the overall training objective is the weighted sum of the above four loss functions:

$$\mathcal{L} = \mathcal{L}_1 + \lambda_1 \mathcal{L}_{fqp} + \lambda_2 \mathcal{L}_{edge} + \lambda_3 (\mathcal{L}_{adv}^G + \mathcal{L}_{adv}^D), \quad (9)$$

where  $\lambda_1, \lambda_2, \lambda_3$  are three hyper-parameters controlling the importance balance of different loss functions. RFormer is end-to-end trained by minimizing  $\mathcal{L}$ . The weights of the perception network are fixed. Each mini-batch training procedure is divided into two steps: (i) Fix the discriminator and train the generator. (ii) Fix the generator and train the discriminator. This adversarial training scheme encourages the reconstructed fundus images to be more photo-realistic and closer to the real clinical HQ fundus image manifold.

## 4. Real Fundus

This section introduces our clinical benchmark, Real Fundus (RF), which consists of 120 LQ and HQ clinical fundus image pairs with the spatial size of  $2560 \times 2560$ . The training and testing subsets are split in proportional to 3:1. Since the blur degradation significantly impacts image analysis, clinical diagnosis and automated image analyzing systems, it is set to the primary degradation type of LQ fundus images. Besides, there are other degradation types such as artifacts and uneven illumination which are inevitably introduced in the fundus image capturing process.

## 4.1. Data Collecting Process

The collection process of our RF contains three steps: capturing, selecting, and calibrating fundus images.

### 4.1.1 Capturing

Instead of exploiting artificial degradation models (*e.g.*, Gaussian Filter.) to synthesize LQ fundus images as shown in Fig. 1 (b), we directly use the LQ fundus images from the fail cases in practical capturing. As depicted in Fig. 1 (a), the fundus images are captured by ophthalmologists using a ZEISS VISUCAM200 fundus camera. We select clinical fundus images from patients of different ages and different fundus states (*e.g.*, leopard fundus, hemorrhage, microaneurysms, and drusen ) to expand the scope of our RF.

### 4.1.2 Selecting

When LQ fundus images are captured in practice, the operator will repeat capturing until HQ fundus images are obtained. Then we manually select LQ and HQ fundus image pairs of the same eye. To ensure the diversity of RF and avoid similar data, only one image pair is selected with one eye. Note that only HQ clear fundus images captured by experienced ophthalmologists can be used as the ground truths of degraded LQ images. Based on these strict criteria, we finally select 120 LQ and HQ fundus image pairs from the eye hospital database containing more than 30,00 eye instances. Each instance contains multiple fundus images.

### 4.1.3 Calibrating

After selecting fundus image pairs, we observe two issues in raw unprocessed fundus data. Firstly, the LQ and HQ fundus images are spatially misaligned (as illustrated in Fig. 1(a)). Secondly, there is a large black area around the eyeball. This black area is uninformative and may easily degrade the performance of the restoration model during the training procedure. Thus, to improve the quality of our RF, we calibrate the collected dataset using the software, Photoshop. Specifically, we first spatially align the image pairs and then cut off the black area around the eyeball.

## 4.2. Comparisons with Synthetic Dataset

### 4.2.1 LQ Fundus Images

We compare the LQ images from our RF and synthetic dataset in Fig. 1 (c). As can be seen from the zoom-in patches that the artificially synthesized degradation is fundamentally different from the real clinical degradation.

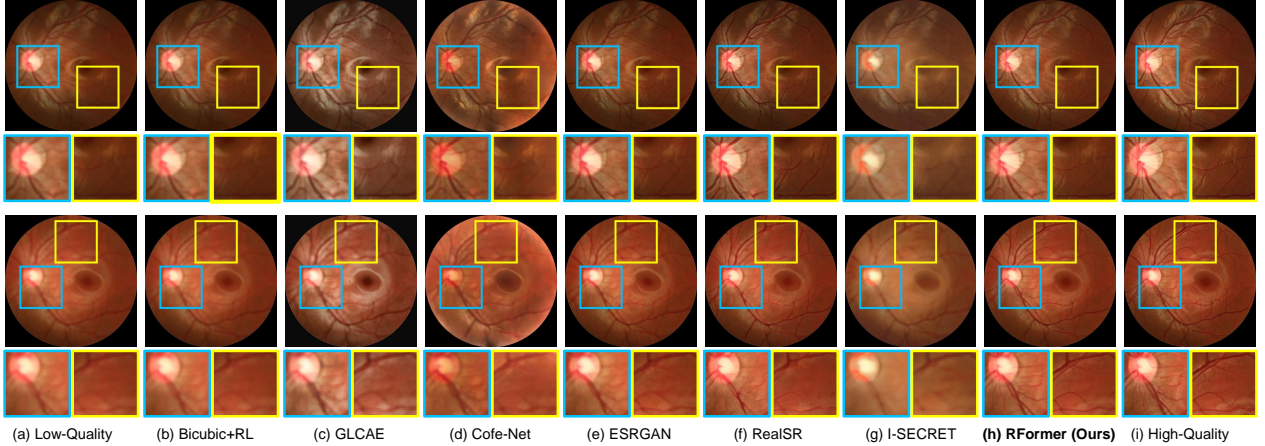


Figure 5. **Restored fundus image comparisons of *Scene 1* on our RF.** Six SOTA methods and our proposed RFormer are included. (a) LQ fundus image. (b) Bicubic+RL [61]. (c) GLCAE [62]. (d) Cofe-Net [58]. (e) ESRGAN [65]. (f) RealSR [33]. (g) I-SECRET [13]. (h) Our proposed RFormer. (i) Ground-truth HQ fundus image. Our RFormer reconstructs more detailed contents and structural textures.

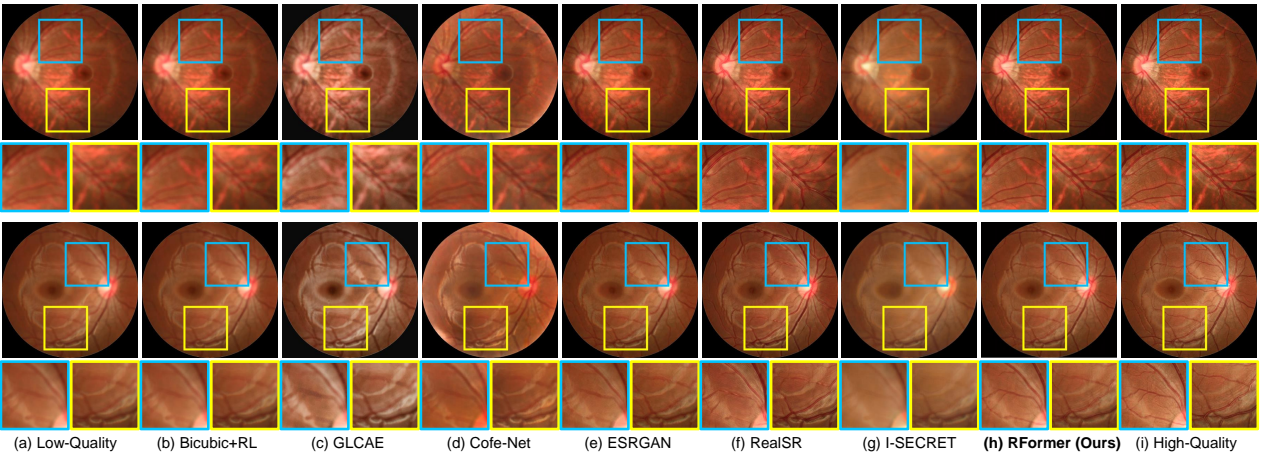


Figure 6. **Restored fundus image comparisons of *Scene 2* on our RF.** Six SOTA methods and our RFormer are included. (a) LQ fundus image. (b) Bicubic+RL [61]. (c) GLCAE [62]. (d) Cofe-Net [58]. (e) ESRGAN [65]. (f) RealSR [33]. (g) I-SECRET [13]. (h) Our proposed RFormer. (i) Ground-truth HQ fundus image. Our RFormer yields more visually pleasant results and restores more edge details.

Table 1. **Quantitative comparisons with SOTA algorithms on our RF.** PSNR, SSIM, Params, and FLOPS are reported.

Method	PSNR	SSIM	Params(M)	FLOPS(G)
Cofe-Net [58]	17.26	0.789	39.31	22.48
GLCAE [62]	21.37	0.570	–	–
I-SECRET [13]	24.57	0.854	10.85	14.21
Bicubic+RL [61]	25.34	0.824	–	–
ESRGAN [65]	26.73	0.823	15.95	18.41
RealSR [33]	27.99	0.850	15.92	29.42
<b>RFormer (Ours)</b>	<b>28.32</b>	<b>0.873</b>	21.11	11.36

#### 4.2.2 Domain Discrepancy

To validate the huge domain discrepancy between the synthetic and real clinical datasets. We adopt two CNN-based fundus image restoration methods, I-SECRET [13] and Cofe-Net [58], to conduct ablation study. We train them with the synthetic data and then test them on our RF. As shown in Fig. 1 (d), the two models fail to reconstruct the

real clinical LQ fundus images. They either yield over-smooth results sacrificing detailed contents, or introduce visually unpleasant artifacts. Since the synthetic data can not be applied to real fundus image restoration, it still remains a severe data-hungry issue. To meet with this research requirement, we establish a large scale clinical dataset, RF. To the best of our knowledge, this is the first work contributing a real clinical fundus image restoration benchmark.

## 5. Experiments

### 5.1. Implementation Details

During the training procedure, fundus images are first cropped into the patches with the size of  $128 \times 128$ . Then the patches are fed into our proposed RFormer. The Adam [36] optimizer ( $\beta_1=0.9$ ,  $\beta_2=0.999$ ) is adopted. The initial learning rate is set to  $1 \times 10^{-4}$  and linearly decreased to  $1 \times 10^{-6}$ .

Table 2. **Ablation Studies.** We train and test all the models on our RF. PSNR, SSIM, Params and FLOPS are reported.

Patch Size	$22 \times 22$	<b><math>40 \times 40</math></b>	$46 \times 46$	$62 \times 62$	$128 \times 128$	Discriminator	PatchGAN	PixelGAN	Pixel and Patch	<b>Ours</b>
PSNR	28.23	<b>28.32</b>	28.12	28.02	28.03	PSNR	27.52	28.00	27.70	<b>28.32</b>
SSIM	0.866	<b>0.873</b>	0.827	0.862	0.796	SSIM	0.822	0.790	0.839	<b>0.873</b>

$\mathcal{L}_{adv}$	$\mathcal{L}_1$	$\mathcal{L}_{fqp}$	$\mathcal{L}_{edge}$	PSNR	SSIM	Window Size	w/o WSAB	$4 \times 4$	<b><math>8 \times 8</math></b>	$16 \times 16$	$32 \times 32$
✓	✓			27.42	0.840	PSNR	14.27	28.23	<b>28.32</b>	27.82	27.63
✓	✓	✓		27.90	0.860	SSIM	0.601	0.873	<b>0.873</b>	0.819	0.812
✓		✓	✓	27.25	0.744	Params(M)	34.53	<b>20.67</b>	21.11	27.54	47.21
✓	✓	✓	✓	28.04	0.858	FLOPS(G)	16.38	<b>10.83</b>	11.36	13.46	18.59
✓	✓		✓	27.25	0.744						
✓	✓	✓	✓	<b>28.32</b>	<b>0.873</b>						

(a) Ablation study of the patch size of our discriminator.

(b) CNN-based vs. our Transformer-based discriminators.

(c) Ablation study of the loss functions.

(d) Ablation study of the window size of our proposed WSAB.

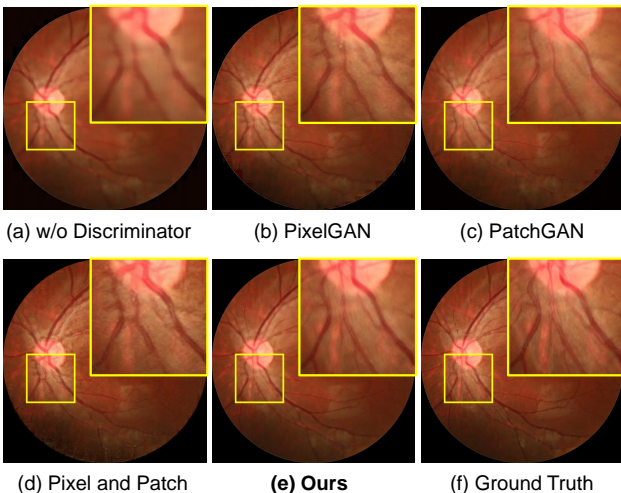


Figure 7. **CNN-based vs. Transformer-based discriminators.**

(a) Without discriminator. (b) CNN-based PixelGAN [32]. (c) CNN-based PatchGAN [32]. (d) CNN-based PixelGAN and PatchGAN. (e) Equipped with our proposed Transformer-based discriminator. (f) Ground truth HQ fundus image. The proposed Transformer-based discriminator significantly surpasses traditional CNN-based discriminators in terms of recovering detailed contents and preserving the anatomical structure consistency.

Our RFormer is implemented by PyTorch. It takes about 12h using an NVIDIA RTX 3090 GPU to train our RFormer for 100 epochs. The mini-batch size is set to 4. Random flipping and rotation are used for data augmentation. We adopt peak signal-to-noise ratio (PSNR) and structural similarity (SSIM) [66] as the metrics to evaluate the performance of fundus image reconstruction.

## 5.2. Comparisons with State-of-the-Art Methods

We provide qualitative and quantitative comparisons between our RFormer with six SOTA methods including two model-based methods (GLCAE [62] and Bicubic+RL [61]) and four CNN-based methods (RealSR [33],

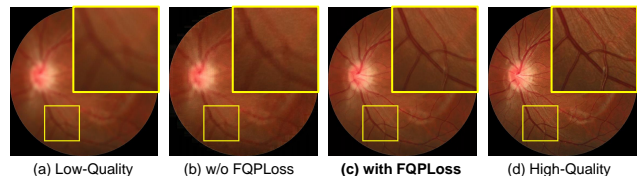


Figure 8. **Ablation study of our FQPLoss.** (a) The LQ fundus image. (b) and (c) depict the images restored by RFormers without and with using FQPLoss, respectively. (d) The ground-truth HQ fundus image. Using our FQPLoss, the model restores more detailed anatomical structure contents and high-frequency textures.

ESRGAN [65], I-SECRET [13], and Cofe-Net [58]). The quantitative comparisons on our RF are shown in Table 1, the proposed RFormer outperforms other competitors in terms of PSNR and SSIM. More specifically, RFormer achieves 0.33 and 1.59 dB improvement in PSNR when compared to RealSR [33] and ESRGAN [65].

Fig. 5 and 6 depict the qualitative comparisons on RF. It can be observed that Bicubic+RL [61], GLCAE [62], I-SECRET [13], and Cofe-Net [58] yield over-smooth results and fail to restore the LQ blurry fundus images. Although ESRGAN [65] and RealSR [33] can reconstruct more high-frequency edge details, they do not maintain the authenticity and anatomical structure of the original fundus. Some undesired artifacts are introduced to the restored images, which may severely mislead the clinical diagnosis. In contrast, our RFormer is capable of restoring more fine-grained contents and structural details without introducing artifacts. Thus, the fundus anatomical structure can be well preserved.

## 5.3. Ablation Study

### 5.3.1 FQPLoss

We adopt RFormer as the restoration model to conduct an ablation study to validate the effect of our FQPLoss. As listed in Table 2 (c), when the FQPLoss is applied, the PSNR and SSIM are increased by 1.07 dB and 0.129, re-

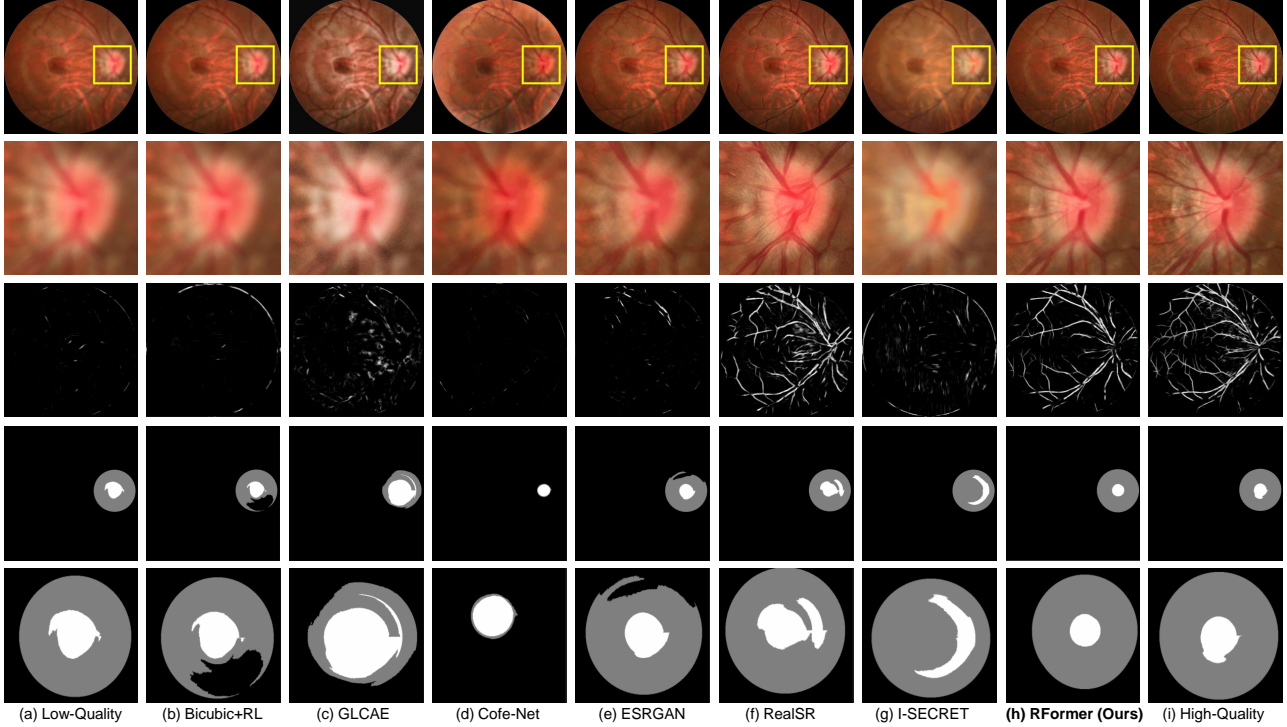


Figure 9. **Vessel segmentation and optic disc/cup detection of *Scene 3* on our RF.** From top to bottom are fundus images, optic disc/cup patches, vessel segmentation maps, optic disc/cup detection maps, and the zoom-in patches of the optic disc/cup detection maps. (a) LQ fundus image. (b) Bicubic+RL [61]. (c) GLCAE [62]. (d) Cofe-Net [58]. (e) ESRGAN [65]. (f) RealSR [33]. (g) I-SECRET [13]. (h) Our RFormer. (i) HQ fundus image. Our method can benefit the clinical analysis on vessel segmentation and optic disc/cup detection.

spectively. In addition, we provide visual comparisons in Fig. 8. As depicted in Fig. 8 (b), the model yields an over-smooth fundus image and fails in reconstructing the fine-grained vessel details without FQPLoss. As shown in Fig. 8 (c), when using our FQPLoss, the model restores more detailed anatomical contents and high-frequency textures.

### 5.3.2 Discriminator

We conduct an ablation study to compare our Transformer-based discriminator with Traditional CNN-based discriminators. The Transformer-based generator remains unchanged. The results are reported in Table 2(b). Compared with the discriminators in CNN-based PatchGAN [32], PixelGAN [32], *etc*, our Transformer-based discriminator yields the best performance. We provide qualitative comparisons in Fig. 7. It can be observed that our Transformer-based discriminator significantly outperforms CNN-based discriminators in terms of recovering detailed contents and preserving the anatomical structure consistency.

### 5.3.3 Patch Size

We experimentally analyze the effect of the patch size set in the Transformer-based discriminator. The results are shown in Table 2 (a). Our RFormer achieves the best restoration

result with the patch size of  $40 \times 40$ .

### 5.3.4 Window Size

We change the window size of W-MSA and conduct experiments to study its effect. The results are reported in Table 2 (d). It can be observed that our RFormer yields the best result when the window size is set to  $8 \times 8$ .

## 5.4. Clinical Image Analysis and Applications

The ultimate goal of restoring and enhancing fundus images is to serve the real clinical tasks better and improve the accuracy of clinical diagnosis. To validate the effectiveness of our proposed RFormer, we use it as a pre-processing technique for downstream clinical image analysis tasks, including vessel segmentation and optic disc/cup detection. LadderNet [83] and M-Net [19] are employed as the segmentation baselines.

### 5.4.1 User Study

Since the restored fundus images should meet the requirements of ophthalmologists, we invite three experienced ophthalmologists to evaluate the quality of images restored by our RFormer and other algorithms [13, 33, 58, 61, 62, 65]. They agree that our method is superior to other compared

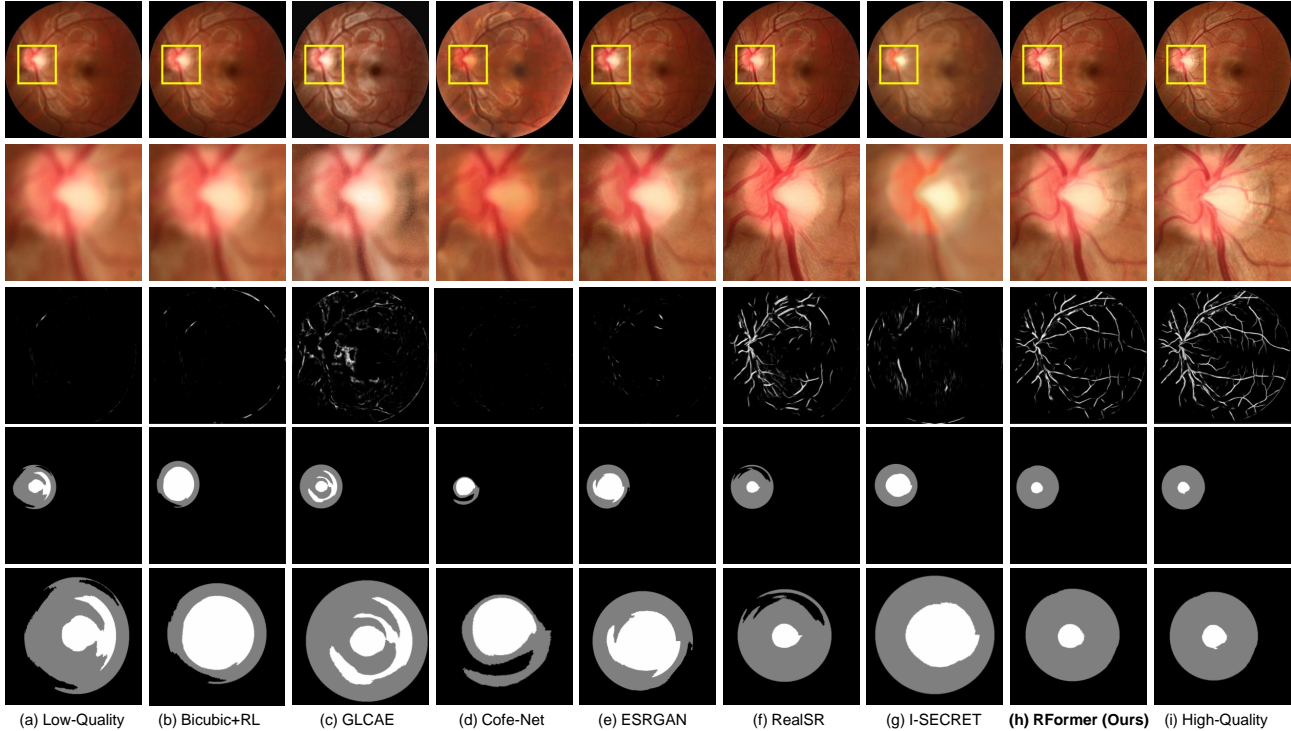


Figure 10. **Vessel segmentation and optic disc/cup detection of *Scene 4* on our RF.** From top to bottom are fundus images, optic disc/cup patches, vessel segmentation maps, optic disc/cup detection maps, and the zoom-in patches of the optic disc/cup detection maps. (a) LQ fundus image. (b) Bicubic+RL [61]. (c) GLCAE [62]. (d) Cofe-Net [58]. (e) ESRGAN [65]. (f) RealSR [33]. (g) I-SECRET [13]. (h) Our RFormer. (i) HQ fundus image. Our method can improve the performance of vessel segmentation and optic disc/cup detection.

restoration methods in LQ fundus image restoration and auxiliary diagnosis of ophthalmic diseases.

#### 5.4.2 Vessel Segmentation

We test LadderNet [83] pre-trained on DRIVE [60] dataset for vessel segmentation on our collected RF. Please note that the vessel segmentation maps of real HQ fundus images serve as the references for comparison due to the lack of segmentation labels on our RF. The vessel segmentation results are shown in the third row of Fig. 9 and 10. As can be seen that LadderNet fails in segmenting the blood vessels of clinical LQ fundus images. In contrast, LadderNet extracts obvious vessel structure of the fundus images restored by our RFormer, which is closest to the segmentation results of real HQ fundus images. These results clearly suggest the effectiveness of our proposed method.

#### 5.4.3 Optic Disc/Cup Detection

We also evaluate the effect of our RFormer for the downstream disc/cup detection task. We test M-Net [19] pre-trained on ORIGA [77] dataset for optic disc/cup detection on our collected RF. Similar to the vessel segmentation task, the optic disc/cup detection results of real HQ fundus images function as the references due to the lack of segmenta-

tion labels. The qualitative comparisons of different fundus image restoration methods are depicted in Fig. 9 and 10. The fourth line is the optic disc/cup detection map and the fifth line depicts the zoom-in patches of the fourth line. It can be observed that M-Net fails to detect the disc/cup on clinical LQ fundus images. On the contrary, M-Net detects the optic cup and disc more accurately on the fundus images reconstructed by our RFormer. This evidence verifies that our method benefits the optic disc/cup detection task.

## 6. Conclusion

In this paper, we establish the first real clinical fundus image restoration benchmark, Real Fundus, which contains LQ and HQ fundus image pairs to alleviate the data-hungry issue. Our dataset can help better evaluate restoration algorithms in clinical scenes. Based on this dataset, we propose a novel Transformer-based method, RFormer, for clinical fundus image restoration. To the best of our knowledge, it is the first attempt to explore the potential of Transformer in this task. Comprehensive qualitative and quantitative results demonstrate that our RFormer significantly outperforms a series of SOTA methods. Extensive experiments verify that the proposed RFormer serving as a data pre-processing technique can boost the performance of different downstream tasks, such as vessel segmentation and

optic disc/cup detection. We hope this work can serve as a baseline for real clinical fundus image restoration and benefit the community of medical imaging.

## References

- [1] Anurag Arnab, Mostafa Dehghani, Georg Heigold, Chen Sun, Mario Lučić, and Cordelia Schmid. Vivit: A video vision transformer. *arXiv preprint arXiv:2103.15691*, 2021. 3
- [2] Philippe Burlina, David E Freund, Neil Joshi, Y Wolfson, and Neil M Bressler. Detection of age-related macular degeneration via deep learning. In *2016 IEEE 13th International Symposium on Biomedical Imaging (ISBI)*, pages 184–188. IEEE, 2016. 1
- [3] Yuanhao Cai, Xiaowan Hu, Haoqian Wang, Yulun Zhang, Hanspeter Pfister, and Donglai Wei. Learning to generate realistic noisy images via pixel-level noise-aware adversarial training. *Advances in Neural Information Processing Systems*, 34, 2021. 3
- [4] Yuanhao Cai, Jing Lin, Xiaowan Hu, Haoqian Wang, Xin Yuan, Yulun Zhang, Radu Timofte, and Luc Van Gool. Mask-guided spectral-wise transformer for efficient hyperspectral image reconstruction. *arXiv preprint arXiv:2111.07910*, 2021. 3
- [5] Yuanhao Cai, Zhicheng Wang, Zhengxiong Luo, Binyi Yin, Angang Du, Haoqian Wang, Xiangyu Zhang, Xinyu Zhou, Erjin Zhou, and Jian Sun. Learning delicate local representations for multi-person pose estimation. In *European Conference on Computer Vision*, pages 455–472. Springer, 2020. 3
- [6] Yuanhao Cai, Zhicheng Wang, Binyi Yin, Ruihao Yin, Angang Du, Zhengxiong Luo, Zeming Li, Xinyu Zhou, Gang Yu, Erjin Zhou, et al. Res-steps-net for multi-person pose estimation. In *Joint COCO and Mapillary Workshop at ICCV*, 2019. 3
- [7] Hu Cao, Yueyue Wang, Joy Chen, Dongsheng Jiang, Xiaopeng Zhang, Qi Tian, and Manning Wang. Swin-unet: Unet-like pure transformer for medical image segmentation. *arXiv preprint arXiv:2105.05537*, 2021. 3
- [8] Jiezhong Cao, Yawei Li, Kai Zhang, and Luc Van Gool. Video super-resolution transformer. *arXiv preprint arXiv:2106.06847*, 2021. 3
- [9] Nicolas Carion, Francisco Massa, Gabriel Synnaeve, Nicolas Usunier, Alexander Kirillov, and Sergey Zagoruyko. End-to-end object detection with transformers. In *European Conference on Computer Vision*, pages 213–229. Springer, 2020. 3
- [10] Hanting Chen, Yunhe Wang, Tianyu Guo, Chang Xu, Yiping Deng, Zhenhua Liu, Siwei Ma, Chunjing Xu, Chao Xu, and Wen Gao. Pre-trained image processing transformer. In *Proceedings of the IEEE/CVF Conference on Computer Vision and Pattern Recognition*, pages 12299–12310, 2021. 3
- [11] Xiangyu Chen, Yanwu Xu, Damon Wing Kee Wong, Tien Yin Wong, and Jiang Liu. Glaucoma detection based on deep convolutional neural network. In *2015 37th annual international conference of the IEEE engineering in medicine and biology society (EMBC)*, pages 715–718. IEEE, 2015. 1
- [12] Yu-Sheng Chen, Yu-Ching Wang, Man-Hsin Kao, and Yung-Yu Chuang. Deep photo enhancer: Unpaired learning for image enhancement from photographs with gans. In *Proceedings of the IEEE Conference on Computer Vision and Pattern Recognition*, pages 6306–6314, 2018. 3
- [13] Pujin Cheng, Li Lin, Yijin Huang, Junyan Lyu, and Xiaoying Tang. I-secret: Importance-guided fundus image enhancement via semi-supervised contrastive constraining. In *International Conference on Medical Image Computing and Computer-Assisted Intervention*, pages 87–96. Springer, 2021. 1, 2, 3, 7, 8, 9, 10
- [14] Xiyang Dai, Yinpeng Chen, Jianwei Yang, Pengchuan Zhang, Lu Yuan, and Lei Zhang. Dynamic detr: End-to-end object detection with dynamic attention. In *Proceedings of the IEEE/CVF International Conference on Computer Vision*, pages 2988–2997, 2021. 3
- [15] Yanyan Dong, Qinyan Zhang, Zhiqiang Qiao, and Ji-Jiang Yang. Classification of cataract fundus image based on deep learning. In *2017 IEEE International Conference on Imaging Systems and Techniques (IST)*, pages 1–5. IEEE, 2017. 1
- [16] Alexey Dosovitskiy, Lucas Beyer, Alexander Kolesnikov, Dirk Weissenborn, Xiaohua Zhai, Thomas Unterthiner, Mostafa Dehghani, Matthias Minderer, Georg Heigold, Sylvain Gelly, et al. An image is worth 16x16 words: Transformers for image recognition at scale. *arXiv preprint arXiv:2010.11929*, 2020. 3
- [17] Alaaeldin El-Nouby, Hugo Touvron, Mathilde Caron, Piotr Bojanowski, Matthijs Douze, Armand Joulin, Ivan Laptev, Natalia Neverova, Gabriel Synnaeve, Jakob Verbeek, et al. Xcit: Cross-covariance image transformers. *arXiv preprint arXiv:2106.09681*, 2021. 3
- [18] Marco Foracchia, Enrico Grisan, and Alfredo Ruggeri. Luminosity and contrast normalization in retinal images. *Medical image analysis*, 9(3):179–190, 2005. 2
- [19] Huazhu Fu, Jun Cheng, Yanwu Xu, Damon Wing Kee Wong, Jiang Liu, and Xiaochun Cao. Joint optic disc and cup segmentation based on multi-label deep network and polar transformation. *IEEE transactions on medical imaging*, 37(7):1597–1605, 2018. 9, 10
- [20] Huazhu Fu, Boyang Wang, Jianbing Shen, Shanshan Cui, Yanwu Xu, Jiang Liu, and Ling Shao. Evaluation of retinal image quality assessment networks in different color-spaces. In *International Conference on Medical Image Computing and Computer-Assisted Intervention*, pages 48–56. Springer, 2019. 5
- [21] Xueyang Fu, Delu Zeng, Yue Huang, Xiao-Ping Zhang, and Xinghao Ding. A weighted variational model for simultaneous reflectance and illumination estimation. In *Proceedings of the IEEE conference on computer vision and pattern recognition*, pages 2782–2790, 2016. 3
- [22] Xinyu Gong, Shiyu Chang, Yifan Jiang, and Zhangyang Wang. Autogan: Neural architecture search for generative adversarial networks. In *Proceedings of the IEEE/CVF International Conference on Computer Vision*, pages 3224–3234, 2019. 3
- [23] Ian Goodfellow, Jean Pouget-Abadie, Mehdi Mirza, Bing Xu, David Warde-Farley, Sherjil Ozair, Aaron Courville, and

- Yoshua Bengio. Generative adversarial nets. *Advances in neural information processing systems*, 27, 2014. 3
- [24] Along He, Tao Li, Ning Li, Kai Wang, and Huazhu Fu. Cabnet: Category attention block for imbalanced diabetic retinopathy grading. *IEEE Transactions on Medical Imaging*, 40(1):143–153, 2020. 1
- [25] Xiaowan Hu, Yuanhao Cai, Zhihong Liu, Haoqian Wang, and Yulun Zhang. Multi-scale selective feedback network with dual loss for real image denoising. In *Proceedings of the Thirtieth International Joint Conference on Artificial Intelligence, IJCAI-21*, pages 729–735. International Joint Conferences on Artificial Intelligence Organization, 2021. 3
- [26] Xiaowan Hu, Yuanhao Cai, Haoqian Wang, Yanbin Peng, and Yulun Zhang.  $Eg^2n$ : enhanced gradient guiding network for single mr image super-resolution. In *Optoelectronic Imaging and Multimedia Technology VII*, volume 11550, page 115500I. International Society for Optics and Photonics, 2020. 3
- [27] Xiaowan Hu, Ruijun Ma, Zhihong Liu, Yuanhao Cai, Xiaole Zhao, Yulun Zhang, and Haoqian Wang. Pseudo 3d auto-correlation network for real image denoising. In *Proceedings of the IEEE/CVF Conference on Computer Vision and Pattern Recognition*, pages 16175–16184, 2021. 3
- [28] Xiaowan Hu, Haoqian Wang, Yuanhao Cai, Xiaole Zhao, and Yulun Zhang. Pyramid orthogonal attention network based on dual self-similarity for accurate mr image super-resolution. In *2021 IEEE International Conference on Multimedia and Expo (ICME)*, pages 1–6. IEEE, 2021. 3
- [29] Cam-Hao Hua, Kiyoungh Kim, Thien Huynh-The, Jong In You, Seung-Young Yu, Thuong Le-Tien, Sung-Ho Bae, and Sungyoung Lee. Convolutional network with twofold feature augmentation for diabetic retinopathy recognition from multi-modal images. *IEEE Journal of Biomedical and Health Informatics*, 2020. 1
- [30] Junjie Huang, Zengguang Shan, Yuanhao Cai, Feng Guo, Yun Ye, Xinze Chen, Zheng Zhu, Guan Huang, Jiwen Lu, and Dalong Du. Coco keypoint challenge track technical report: Udp++. In *Joint COCO and LVIS Workshop at ECCV 2020*, 2020. 3
- [31] Sung Ju Hwang, Ashish Kapoor, and Sing Bing Kang. Context-based automatic local image enhancement. In *European conference on computer vision*, pages 569–582. Springer, 2012. 2
- [32] Phillip Isola, Jun-Yan Zhu, Tinghui Zhou, and Alexei A Efros. Image-to-image translation with conditional adversarial networks. In *Proceedings of the IEEE conference on computer vision and pattern recognition*, pages 1125–1134, 2017. 3, 4, 8, 9
- [33] Xiaozhong Ji, Yun Cao, Ying Tai, Chengjie Wang, Jilin Li, and Feiyue Huang. Real-world super-resolution via kernel estimation and noise injection. In *Proceedings of the IEEE/CVF Conference on Computer Vision and Pattern Recognition Workshops*, pages 466–467, 2020. 7, 8, 9, 10
- [34] Yifan Jiang, Shiyu Chang, and Zhangyang Wang. Transgan: Two pure transformers can make one strong gan, and that can scale up. *Advances in Neural Information Processing Systems*, 34, 2021. 3
- [35] Yifan Jiang, Xinyu Gong, Ding Liu, Yu Cheng, Chen Fang, Xiaohui Shen, Jianchao Yang, Pan Zhou, and Zhangyang Wang. Enlightengan: Deep light enhancement without paired supervision. *IEEE Transactions on Image Processing*, 30:2340–2349, 2021. 3
- [36] Diederik P. Kingma and Jimmy Lei Ba. Adam: A method for stochastic optimization. In *ICLR*, 2015. 7
- [37] Christian Ledig, Lucas Theis, Ferenc Huszár, Jose Caballero, Andrew Cunningham, Alejandro Acosta, Andrew Aitken, Alykhan Tejani, Johannes Totz, Zehan Wang, et al. Photo-realistic single image super-resolution using a generative adversarial network. In *Proceedings of the IEEE conference on computer vision and pattern recognition*, pages 4681–4690, 2017. 3
- [38] Chuan Li and Michael Wand. Combining markov random fields and convolutional neural networks for image synthesis. In *Proceedings of the IEEE conference on computer vision and pattern recognition*, pages 2479–2486, 2016. 3
- [39] Ke Li, Shijie Wang, Xiang Zhang, Yifan Xu, Weijian Xu, and Zhuowen Tu. Pose recognition with cascade transformers. In *Proceedings of the IEEE/CVF Conference on Computer Vision and Pattern Recognition*, pages 1944–1953, 2021. 3
- [40] Runde Li, Jinshan Pan, Zechao Li, and Jinhui Tang. Single image dehazing via conditional generative adversarial network. In *Proceedings of the IEEE Conference on Computer Vision and Pattern Recognition*, pages 8202–8211, 2018. 3
- [41] Yanjie Li, Shoukui Zhang, Zhicheng Wang, Sen Yang, Wankou Yang, Shu-Tao Xia, and Erjin Zhou. Tokenpose: Learning keypoint tokens for human pose estimation. *arXiv preprint arXiv:2104.03516*, 2021. 3
- [42] Jingyun Liang, Jiezhong Cao, Guolei Sun, Kai Zhang, Luc Van Gool, and Radu Timofte. Swinir: Image restoration using swin transformer. In *Proceedings of the IEEE/CVF International Conference on Computer Vision*, pages 1833–1844, 2021. 3
- [43] WangMin Liao, BeiJi Zou, RongChang Zhao, YuanQiong Chen, ZhiYou He, and MengJie Zhou. Clinical interpretable deep learning model for glaucoma diagnosis. *IEEE journal of biomedical and health informatics*, 24(5):1405–1412, 2019. 1
- [44] Ze Liu, Yutong Lin, Yue Cao, Han Hu, Yixuan Wei, Zheng Zhang, Stephen Lin, and Baining Guo. Swin transformer: Hierarchical vision transformer using shifted windows. *arXiv preprint arXiv:2103.14030*, 2021. 3, 4, 5
- [45] Yuhao Luo, Kun Chen, Lei Liu, Jicheng Liu, Jianbo Mao, Genjie Ke, and Mingzhai Sun. Dehaze of cataractous retinal images using an unpaired generative adversarial network. *IEEE Journal of Biomedical and Health Informatics*, 24(12):3374–3383, 2020. 2, 3
- [46] Zhengxion Luo, Zhicheng Wang, Yuanhao Cai, Guan Wang, Liang Wang, Yan Huang, ErJin Zhou, Tieniu Tan, and Jian Sun. Efficient human pose estimation by learning deeply aggregated representations. In *2021 IEEE International Conference on Multimedia and Expo (ICME)*, pages 1–6. IEEE, 2021. 3
- [47] Dwarikanath Mahapatra, Behzad Bozorgtabar, and Rahil Garnavi. Image super-resolution using progressive genera-

- tive adversarial networks for medical image analysis. *Computerized Medical Imaging and Graphics*, 71:30–39, 2019. [2](#), [3](#)
- [48] Sharmin Majumder and Nasser Kehtarnavaz. Multitasking deep learning model for detection of five stages of diabetic retinopathy. *arXiv preprint arXiv:2103.04207*, 2021. [1](#)
- [49] Nooshin Mojab, Vahid Noroozi, S Yu Philip, and Joelle A Hallak. Deep multi-task learning for interpretable glaucoma detection. In *2019 IEEE 20th International Conference on Information Reuse and Integration for Data Science (IRI)*, pages 167–174. IEEE, 2019. [1](#)
- [50] Michael K Ng and Wei Wang. A total variation model for retinex. *SIAM Journal on Imaging Sciences*, 4(1):345–365, 2011. [3](#)
- [51] Yifan Peng, Shazia Dharssi, Qingyu Chen, Tiarnan D Keenan, Elvira Agrón, Wai T Wong, Emily Y Chew, and Zhiyong Lu. Deepseenet: a deep learning model for automated classification of patient-based age-related macular degeneration severity from color fundus photographs. *Ophthalmology*, 126(4):565–575, 2019. [1](#)
- [52] Sam Philip, LM Cowie, and JA Olson. The impact of the health technology board for scotland’s grading model on referrals to ophthalmology services. *British Journal of Ophthalmology*, 89(7):891–896, 2005. [1](#)
- [53] Rui Qian, Robby T Tan, Wenhan Yang, Jiajun Su, and Jiaying Liu. Attentive generative adversarial network for rain-drop removal from a single image. In *Proceedings of the IEEE conference on computer vision and pattern recognition*, pages 2482–2491, 2018. [3](#)
- [54] Hina Raja, Taimur Hassan, Muhammad Usman Akram, and Naoufel Werghi. Clinically verified hybrid deep learning system for retinal ganglion cells aware grading of glaucomatous progression. *IEEE Transactions on Biomedical Engineering*, 2020. [1](#)
- [55] Olaf Ronneberger, Philipp Fischer, and Thomas Brox. U-net: Convolutional networks for biomedical image segmentation. In *International Conference on Medical image computing and computer-assisted intervention*, pages 234–241. Springer, 2015. [4](#)
- [56] Sourya Sengupta, Alexander Wong, Amitojdeep Singh, John Zelek, and Vasudevan Lakshminarayanan. Desupgan: multi-scale feature averaging generative adversarial network for simultaneous de-blurring and super-resolution of retinal fundus images. In *International Workshop on Ophthalmic Medical Image Analysis*, pages 32–41. Springer, 2020. [2](#), [3](#)
- [57] Agung W Setiawan, Tati R Mengko, Oerip S Santoso, and Andriyan B Suksmono. Color retinal image enhancement using clahe. In *International Conference on ICT for Smart Society*, pages 1–3. IEEE, 2013. [3](#)
- [58] Ziyi Shen, Huazhu Fu, Jianbing Shen, and Ling Shao. Modeling and enhancing low-quality retinal fundus images. *IEEE Transactions on Medical Imaging*, 40(3):996–1006, 2020. [1](#), [2](#), [3](#), [7](#), [8](#), [9](#), [10](#)
- [59] Karen Simonyan and Andrew Zisserman. Very deep convolutional networks for large-scale image recognition. *arXiv preprint arXiv:1409.1556*, 2014. [5](#)
- [60] Joes Staal, Michael D Abràmoff, Meindert Niemeijer, Max A Viergever, and Bram Van Ginneken. Ridge-based vessel segmentation in color images of the retina. *IEEE transactions on medical imaging*, 23(4):501–509, 2004. [10](#)
- [61] Yu-Wing Tai, Ping Tan, and Michael S Brown. Richardson-lucy deblurring for scenes under a projective motion path. *IEEE Transactions on Pattern Analysis and Machine Intelligence*, 33(8):1603–1618, 2010. [7](#), [8](#), [9](#), [10](#)
- [62] Qi-Chong Tian and Laurent D Cohen. Global and local contrast adaptive enhancement for non-uniform illumination color images. In *Proceedings of the IEEE International Conference on Computer Vision Workshops*, pages 3023–3030, 2017. [7](#), [8](#), [9](#), [10](#)
- [63] Ashish Vaswani, Noam Shazeer, Niki Parmar, Jakob Uszkoreit, Llion Jones, Aidan N Gomez, Łukasz Kaiser, and Illia Polosukhin. Attention is all you need. In *Advances in neural information processing systems*, pages 5998–6008, 2017. [2](#), [3](#)
- [64] Wei Wang and Michael K Ng. A nonlocal total variation model for image decomposition: illumination and reflectance. *Numerical Mathematics: Theory, Methods and Applications*, 7(3):334–355, 2014. [3](#)
- [65] Xintao Wang, Ke Yu, Shixiang Wu, Jinjin Gu, Yihao Liu, Chao Dong, Yu Qiao, and Chen Change Loy. Esrgan: Enhanced super-resolution generative adversarial networks. In *Proceedings of the European conference on computer vision (ECCV) workshops*, pages 0–0, 2018. [3](#), [7](#), [8](#), [9](#), [10](#)
- [66] Zhou Wang, Alan C Bovik, Hamid R Sheikh, and Eero P Simoncelli. Image quality assessment: from error visibility to structural similarity. *IEEE transactions on image processing*, 13(4):600–612, 2004. [8](#)
- [67] Zhendong Wang, Xiaodong Cun, Jianmin Bao, and Jianzhuang Liu. Uformer: A general u-shaped transformer for image restoration. *arXiv preprint arXiv:2106.03106*, 2021. [3](#)
- [68] Bryan M Williams, Baidaa Al-Bander, Harry Pratt, Samuel Lawman, Yitian Zhao, Yalin Zheng, and Yaochun Shen. Fast blur detection and parametric deconvolution of retinal fundus images. In *Fetal, Infant and Ophthalmic Medical Image Analysis*, pages 194–201. Springer, 2017. [2](#), [3](#)
- [69] Bichen Wu, Chenfeng Xu, Xiaoliang Dai, Alvin Wan, Peizhao Zhang, Zhicheng Yan, Masayoshi Tomizuka, Joseph Gonzalez, Kurt Keutzer, and Peter Vajda. Visual transformers: Token-based image representation and processing for computer vision. *arXiv preprint arXiv:2006.03677*, 2020. [3](#)
- [70] Sen Yang, Zhibin Quan, Mu Nie, and Wankou Yang. Transpose: Keypoint localization via transformer. In *Proceedings of the IEEE/CVF International Conference on Computer Vision*, pages 11802–11812, 2021. [3](#)
- [71] Shuai Yang, Zhangyang Wang, Jiaying Liu, and Zongming Guo. Deep plastic surgery: Robust and controllable image editing with human-drawn sketches. In *European Conference on Computer Vision*, pages 601–617. Springer, 2020. [3](#)
- [72] Shuai Yang, Zhangyang Wang, Zhaowen Wang, Ning Xu, Jiaying Liu, and Zongming Guo. Controllable artistic text

- style transfer via shape-matching gan. In *Proceedings of the IEEE/CVF International Conference on Computer Vision*, pages 4442–4451, 2019. 3
- [73] Wenhan Yang, Shiqi Wang, Yuming Fang, Yue Wang, and Jiaying Liu. From fidelity to perceptual quality: A semi-supervised approach for low-light image enhancement. In *Proceedings of the IEEE/CVF Conference on Computer Vision and Pattern Recognition*, pages 3063–3072, 2020. 3
- [74] Jiahui Yu, Zhe Lin, Jimei Yang, Xiaohui Shen, Xin Lu, and Thomas S Huang. Generative image inpainting with contextual attention. In *CVPR*, 2018. 3
- [75] Yuan Yuan, Siyuan Liu, Jiawei Zhang, Yongbing Zhang, Chao Dong, and Liang Lin. Unsupervised image super-resolution using cycle-in-cycle generative adversarial networks. In *Proceedings of the IEEE Conference on Computer Vision and Pattern Recognition Workshops*, pages 701–710, 2018. 3
- [76] Hongyan Zhang, Kai Niu, Yanmin Xiong, Weihua Yang, ZhiQiang He, and Hongxin Song. Automatic cataract grading methods based on deep learning. *Computer methods and programs in biomedicine*, 182:104978, 2019. 1
- [77] Zhuo Zhang, Feng Shou Yin, Jiang Liu, Wing Kee Wong, Ngan Meng Tan, Beng Hai Lee, Jun Cheng, and Tien Yin Wong. Origa-light: An online retinal fundus image database for glaucoma analysis and research. In *2010 Annual International Conference of the IEEE Engineering in Medicine and Biology*, pages 3065–3068. IEEE, 2010. 10
- [78] He Zhao, Bingyu Yang, Lvchen Cao, and Huiqi Li. Data-driven enhancement of blurry retinal images via generative adversarial networks. In *International Conference on Medical Image Computing and Computer-Assisted Intervention*, pages 75–83. Springer, 2019. 2, 3
- [79] Chuanxia Zheng, Tat-Jen Cham, and Jianfei Cai. Pluralistic image completion. In *Proceedings of the IEEE/CVF Conference on Computer Vision and Pattern Recognition*, pages 1438–1447, 2019. 3
- [80] Sixiao Zheng, Jiachen Lu, Hengshuang Zhao, Xiatian Zhu, Zekun Luo, Yabiao Wang, Yanwei Fu, Jianfeng Feng, Tao Xiang, Philip HS Torr, et al. Rethinking semantic segmentation from a sequence-to-sequence perspective with transformers. In *Proceedings of the IEEE/CVF Conference on Computer Vision and Pattern Recognition*, pages 6881–6890, 2021. 3
- [81] Jun-Yan Zhu, Taesung Park, Phillip Isola, and Alexei A Efros. Unpaired image-to-image translation using cycle-consistent adversarial networks. In *Proceedings of the IEEE international conference on computer vision*, pages 2223–2232, 2017. 3
- [82] Xizhou Zhu, Weijie Su, Lewei Lu, Bin Li, Xiaogang Wang, and Jifeng Dai. Deformable detr: Deformable transformers for end-to-end object detection. *arXiv preprint arXiv:2010.04159*, 2020. 3
- [83] Juntang Zhuang. Laddernet: Multi-path networks based on u-net for medical image segmentation. *arXiv preprint arXiv:1810.07810*, 2018. 9, 10